CHEMISTRY of MATERIALS

VOLUME 10, NUMBER 11 NOVEMBER 1998

Reviews

Nanoparticles of Layered Compounds with Hollow Cage Structures (Inorganic Fullerene-Like Structures)†

R. Tenne,* M. Homyonfer, and Y. Feldman

Department of Materials and Interfaces, Weizmann Institute, Rehovot 76100, Israel

Received March 31, 1998. Revised Manuscript Received July 13, 1998

Using the paradigm of carbon fullerenes, it is shown that nanoparticles of inorganic compounds with a layered structure, like MoS_2, are unstable against bending and form hollow closed clusters, designated *inorganic fullerene-like structures* (IF). The analogy can be extended to similar nanostructures, like nanotubes (NT), nested fullerenes, fullerenes with negative curvature (Schwartzites), etc. Various synthetic routes are described to obtain isolated phases of IF. Pentagons and heptagons are expected to play a primordial role in the folding of these nanostructures but no direct evidence for their presence or their detailed structure exists so far. Depending on the structure of the unit cell of the layered compound, apexes of a different topology, like triangles or rectangles, are believed to be stable elements in IF. Applications of such nanoparticles as solid lubricants in mixtures with lubricating fluids are described.

Contents

I. Introduction

Folding of chemical compounds and formation of hollow cage polyhedra, has been already discussed during the early thirties by Pauling,[1] who investigated the formation mechanism of hollow asbestos whiskers. He observed, that naturally occurring minerals, such as Kaolinite (Figure 1), which are composed of alumina octahedra on one side and silica tetrahedra on the other

† **In memory:** The October issue of *Chemistry of Materials* was dedicated to Prof. Jean Rouxel, a great solid-state chemist and a dear friend who left us in an untimely manner. Listening to Jean was always a privilege for me (R.T.) because it left me with the feeling of learning something new in solid-state chemistry and a great desire to learn more from him. His special talent to discuss in his papers new principles of solid-state chemistry in pedagogical, yet in a profound way was a source of continued encouragement for me. I will miss the long hours of discussions around the dining table during which his broad culture and deep understanding of fundamental issues in history of humanity, art, and philosophy were revealed. His legacy will remain among his many students and colleagues for many years to come.

10.1021/cm9802189 CCC: $15.00
Published on Web 10/08/1998

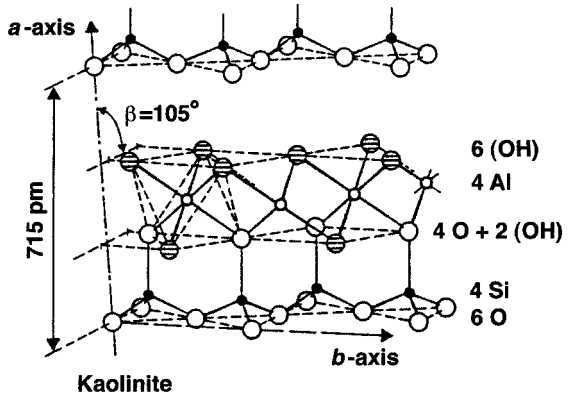

Figure 1. Schematic drawing of the kaolinite unit cell. The inclination along the *c*-axis, which stems from unequal *b*-axis for the two sub-lattices, is responsible for the folding of the lattice and formation of hollow whiskers.

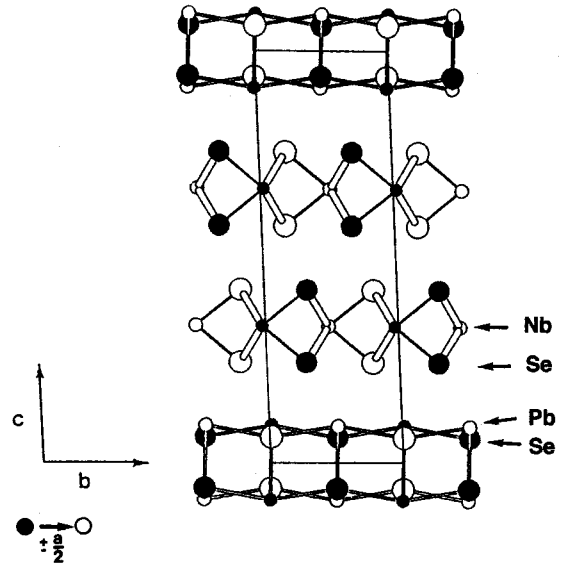

Figure 2. Schematic drawing of the unit cell of the synthetic "misfit" compound $NbSe_2$−PbSe.[2b] Note the inclination of the unit cell along the *c*-axis due to unequal *b*-axis of the two sub-lattices.

side of the unit cell, are asymmetric along the *c*-axis and consequently they prefer to fold and adopt a hollow fiber structure. In analogy to the naturally occurring minerals, the so-called "misfit compounds" with a similar asymmetry along the *c*-axis (see Figure 2) were synthesized and investigated in various laboratories.[2] Some of the compounds belonging to this category exhibit lattice mismatch in the *b*-axis and therefore their unit cell is inclined along the *c*-axis. Consequently, they crystallize in either platelet form or as hollow whiskers (see Figure 3). Incidentally, this observation led Pauling[1] to conclude that compounds that do not exhibit such asymmetry, like MoS_2 and $CdCl_2$, will not be able to form a hollow cage structure.

Until recently, boron was considered to be the element with the largest number of cage structures and, hence, the richest chemistry of polyhedral structures has been worked-out with boron. Figure 4 shows a number of such polyhedral structures. The structure and properties of borohydride polyhedra (boranes) have been elucidated in detail in the past by Lipscomb[3] and others.

The idea that nanocrystalline phases of a given material may adopt a radically different lattice structure

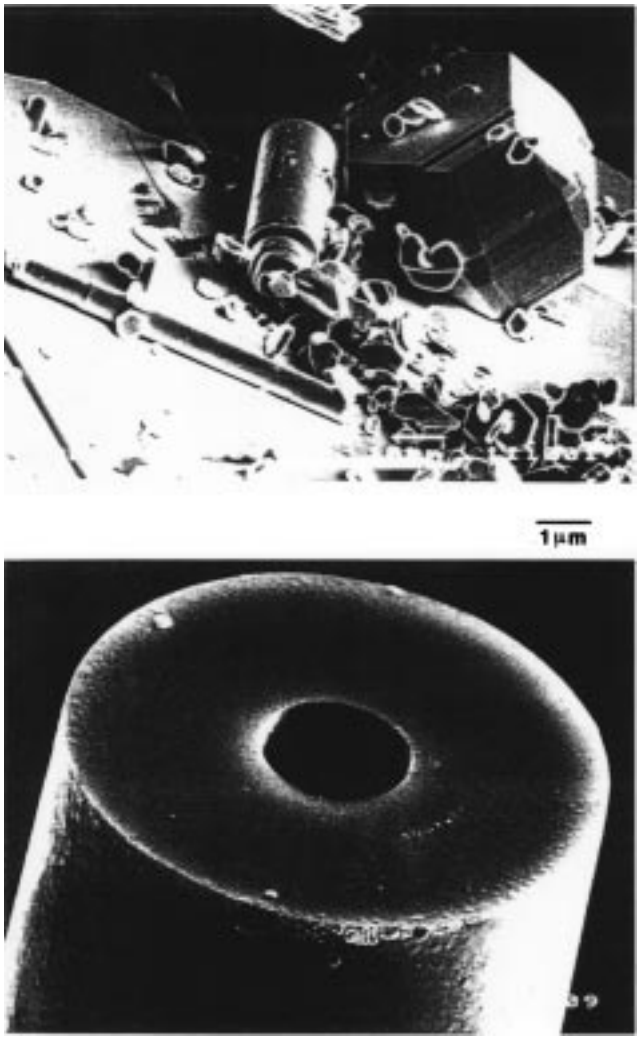

Figure 3. Scanning electron microscopy image of a group of platelets and hollow whiskers of the "misfit" compound TaS_2−SmS.[2d] Note that the material can crystallize in both platelet shape and as a hollow whisker.

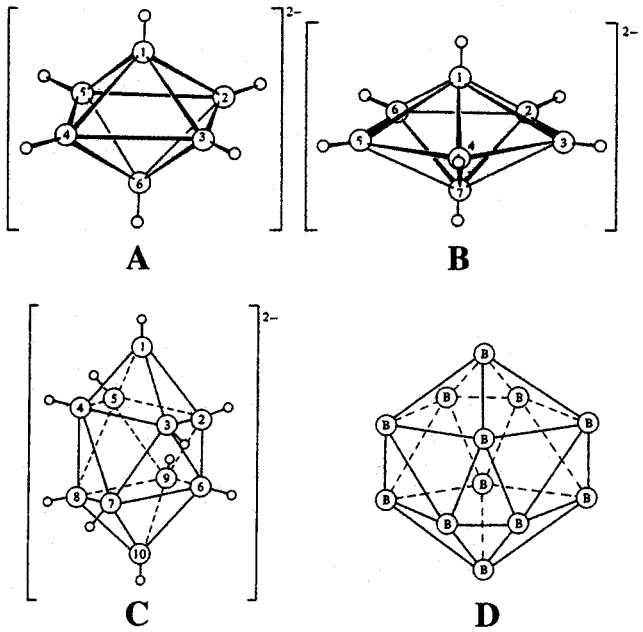

Figure 4. Representation of boranes polyhedra. Hollow circles represent hydrogen atoms.

from the bulk solid, is not new either. The mathematical basis for this kind of transformation was developed in the early sixties.[4] Based on evidence from X-ray diffraction studies, it was concluded that amorphous metals (and metal alloys) consist of icosahedral clusters that have distinctly different structure from the face-centered cubic (fcc) lattice of the bulk material.[5−7] Supercooling of liquid metals was attributed to the prevalence of 13-atom icosahedral clusters near the freezing point.[8] These clusters are responsible for the delayed crystallization of bulk fcc metallic crystallites. Analogous transformations of certain metal alloys into an amorphous phase consisting of icosahedral nanoclusters occurs under pressure.[9] Nanocrystals of sizable dimensions (up to ∼10 nm), in which each atom preserves its distorted sp^3 structure but the crystals have a superstructure of multiple twinned dodecahedral or icosahedral symmetry,[10−13] were observed by transmission electron microscopy (TEM) for some metals (Au, Ag, Ni, Mg) and crystallites of rare gases, like Ar,[14] obtained at low temperatures. The small lattice distortion (5%) caused by such rearrangements leads to an elastic strain that is more than compensated for by the large gain in cohesive energy of the cluster, due to the larger average coordination number of the atoms. For larger crystallites, a macroscopic gap opens between the twins of the crystallites, which render them unstable with respect to the fcc bulk structure.[13] Theoretical calculations have indicated that metallic clusters, (<2000 atoms) are most stable in the icosahedral structure.[15,16] Above this size, a range of intermediate structures was proposed. The same theory has shown that the fcc lattice is stable for crystallites larger than ∼20 000 atoms. The phase change of a nanoparticle (e.g., icosahedral to cubooctahedral transformation) is nondiffusive in nature (i.e., small rearrangements of the atoms is sufficient to transform the lattice from one structure to another). In other cases (Pd, Pt, Cu), however, the nanoparticles adopted the same structure as the bulk solid (fcc).[17] Macroscopic B_6O crystallites, which consist of a hierarchy of icosahedral clusters, have been recently reported.[18]

Among nanophase materials, the fullerenes occupy a special place, primarily because of the high symmetry and the unique hollow-cage topologies that are exhibited by these moieties. The propensity of graphite nanoclusters to form the C_{60} molecule (see Figure 5) has been attributed to the large surface energy of the peripheral sp^2 (2-fold) bonded carbon atoms. Introducing five-membered rings into the hexagonal network structure of graphite induces bending and strain into the structure. The strain is responsible for a kinetic barrier, which can be overcome by heating the nanoclusters or other means of excitation. The extreme stability of the C_{60} molecule (Figure 6) was attributed to the fact that this is the smallest carbon cluster with 12 disjoint pentagons.[19] The discovery of the C_{60} molecule stimulated scientists to search for other related forms of carbon and reinterpret older data in terms of the new concept of carbon cage structures. Even prior to the discovery of the C_{60} molecule, Iijima[20] had proposed that carbon "onions" (nested fullerenes; see Figure 7A) consist of multiple carbon cages, each with 12 pentagonal rings disposed in the carbon hexagonal (graphite)

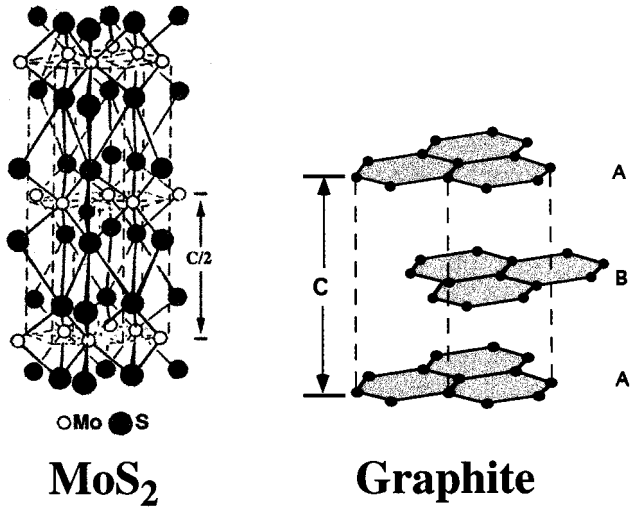

Figure 5. Schematic drawings of graphite and MoS_2 nanoclusters. Note that in both cases the surface energy, which destabilizes the planar topology of the nanocluster, is concentrated in the edge planes parallel to the *c*-axis (||*c*).

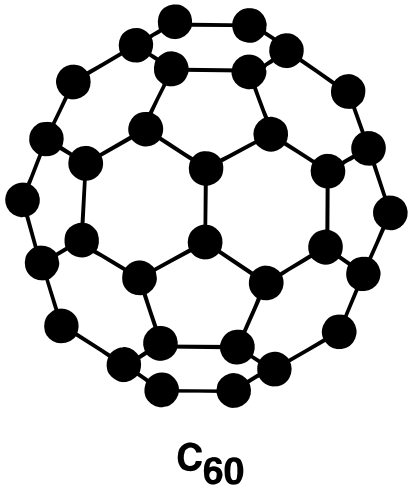

Figure 6. Illustrative picture of the C_{60} molecule (front surface only).

network. Later, the same author realized that the formerly observed carbon nanotubes consist of a folded graphene (single graphite sheet) capped by a hemispherical fullerene (6 pentagons only) on each side.[21] Soon after this discovery, negative (Gaussian) curvature was attributed to the existence of seven-membered rings in the hexagonal network.[22] At this stage, and in particular after the procedures for the synthesis of macroscopic amounts of C_{60}[23] and later on of nanotubes[24] were elucidated, it became clear that a new and exciting world of closed cages carbon chemistry had been spawned and the pace of new discoveries went on unabated for a number of years.

In a related work, Castelman and co-workers found that Ti and C, which crystallize as fcc with a 1:1 ratio between the two atoms in the bulk, adopt a hollow cage structure consisting of 12 pentagons with truncated icosahedral symmetry of the composition Ti_8C_{12} in nanoscopic phases.[25] The so-called metallocarbohedrene (Met-Cars) clusters were observed to be the stable form of a number of transition-metal carbon nanophases[26] that crystallize in fcc lattice in the bulk.

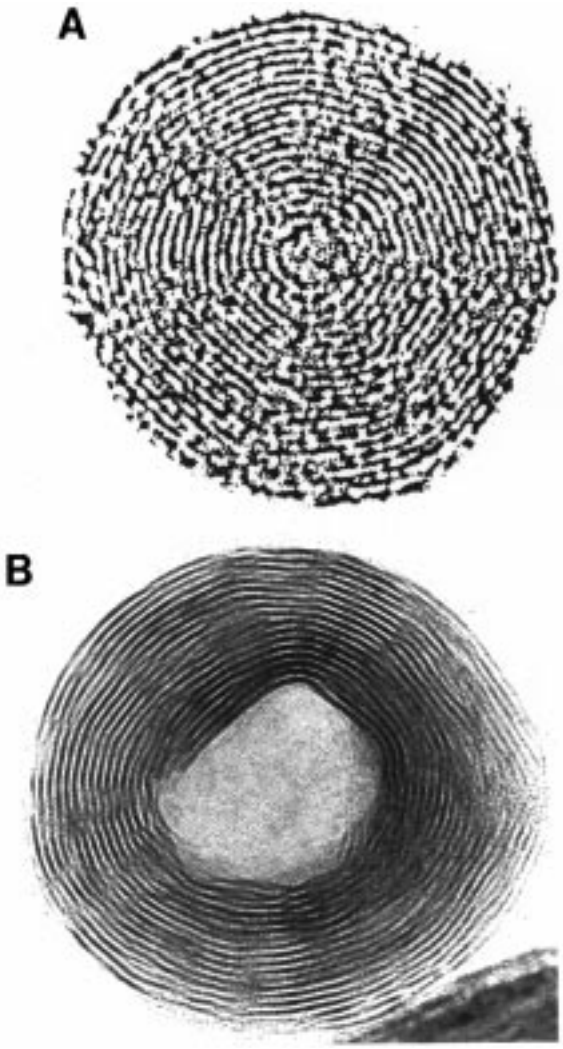

Figure 7. TEM lattice images of carbon-nested fullerene (A) and IF−WS_2 (B). Each dark line represents an atomic layer of the basal plane (0001). The distance between each two layers is 3.35 and 6.18 Å for carbon-nested fullerene and IF−WS_2, respectively. The *c*-axis is always normal to the surface of the nested fullerenes in both cases.

In analogy to graphite, materials with a quasi-two-dimensional (2-D) character (layered compounds), like MoS_2, do not expose dangling bonds on the basal (0001) plane ($\perp c$), which manifests itself through very inert and low energy (0001) surface (Figure 5). Contrarily, the dangling bonds of the prismatic ($11\bar{2}0$) face perpendicular to the basal plane ($\parallel c$), are very reactive. Therefore, nanoclusters of 2-D materials, which have large fraction of their atoms on the prismatic edges with unsaturated bonds, are inherently unstable in the planar structure. Consequently, these materials form hollow-cage nanostructures, that are free of dangling bonds. This analogy between carbon and 2-D (layered) compounds was pointed out initially for WS_2 nanoclusters[27] and later for MoS_2[28] and the respective selenides.[29] To date, there are a few families of 2-D compounds that were shown to adopt fullerene-like structures or form nanotubes. To underline the fact that these fullerene-like structures are derived from inorganic compounds with a 2-D character, they were designated *inorganic fullerene-like materials* (IF).

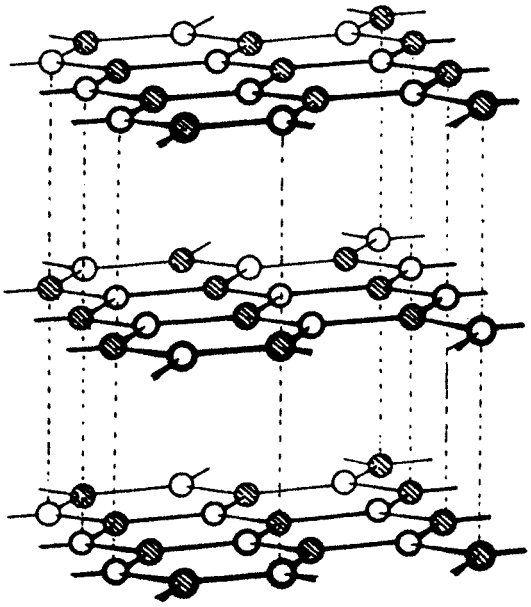

Figure 8. Crystal structure of hexagonal (graphitic) boronitride.

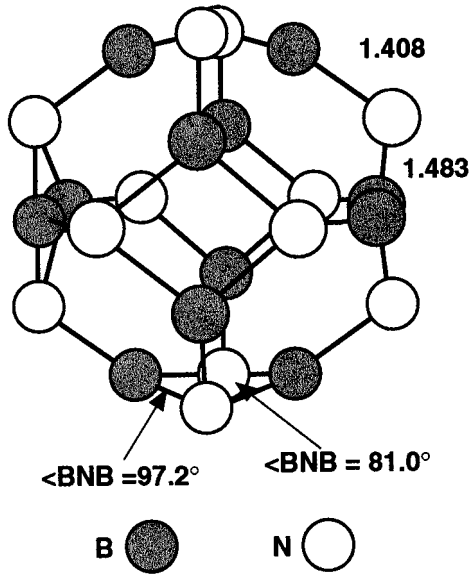

Figure 9. Structure of $(BN)_{12}$ truncated octahedron.[33a]

Because boron nitride (BN) crystallizes in a graphite-like structure (Figure 8) it is natural to consider it as a precursor for the formation of BN fullerenic structures. Replacement of pairs of carbon atoms by the isoelectronic B−N pairs in the hollow cage structure of C_{60}, etc., and in carbon nanotubes was predicted[30] and later verified experimentally.[31,32] This replacement may lead to various mixed $C_{60-2n}N_nB_n$ and even pure B_nN_{60-n} structures. However, pairs of B−B or N−N neighboring atoms, which occur on rings with odd number of atoms (like five- and seven-member rings), may destabilize the closed cage and the nanotube cap and lead to a chemical frustration. Therefore, hollow cage structures with rings with an even number of atoms, such as $(BN)_{12}$, which consists of eight six-membered and six four-membered rings arranged in octahedral symmetry (see Figure 9) were proposed as the stable moieties.[33] In fact, the replacement of any number of C−C pairs by B−N pairs in the hexagonal network of graphite leads

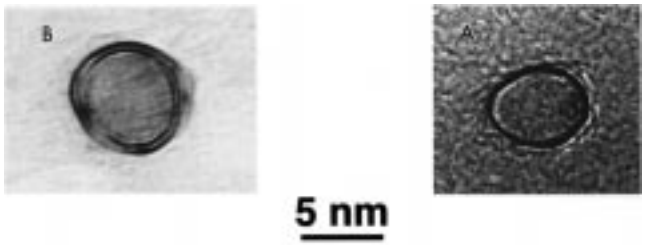

Figure 10. Single-wall (A) and double-wall (B) IF−MoS_2 structures synthesized through the gas-phase reaction between MoO_{3-x} and H_2S.

to a whole array of 2-D phases that can potentially form hollow cage structures and nanotubes. This is another manifestation of the same principle that promotes nanoclusters of 2-D phases to form hollow cage structures.

II. Typical IF Structures of Metal Dichalcogenides

In analogy to carbon fullerenes, the stimulus for the formation of hollow cage structures of these compounds was thought to emanate from the dangling bonds on the prismatic face ($\|c$) of the metal dichalcogenide (MX_2) nanocluster (Figure 5). The deviations from planarity of the nanocluster during the early stages of the formation of a hollow cage structure is an endrogenic process due to the elastic strain involved in tilting the chemical bonds. Therefore, a source of energy input was found to increase the yield of the synthesis of carbon fullerenes.[34] Realizing the importance of these two issues, we synthesized such hollow cage structures by firing a thin (discontinuous) film of tungsten in H_2S atmosphere under strongly reducing conditions, which shift the chemical equilibrium in favor of the MX_2 compound.[27−29] Figure 7B shows high-resolution image of a typical WS_2 "onion". Single- and double-layer fullerene-like particles have been synthesized as well and are shown in Figure 10. The analogy to carbon fullerenes "onions", and nanotubes is compelling.

In contrast to the carbon structures, the detailed structure of IF-MS_2 is not clear. In particular, the existence of pentagonal rings was not confirmed and the detailed structure of the nanocluster is not yet understood. To achieve this goal, hollow cage nanoclusters of precise masses must be prepared and analyzed, and their structure, which has eluded the community thus far, be elucidated.

Disposition of heptagonal rings in the graphite network was shown to lead to structures with negative curvature.[35,36] In analogy to the negative curvature that was indicated in the case of carbon fullerenes, structures with negative curvature were also found to occur in IF−MoS_2.[37,38] Thus MoS_2 T-bars (Figure 11), which are likely to contain heptagonal rings in the neck and even a complete torous were observed.[37] WS_2 hollow coils (Figure 12), presumably with a few heptagon (inner wall)−pentagon (outer wall) pairs per pitch, were reported as well.[38]

The occurrence of an extra sulfur (tungsten) atom in the middle of the hexagonal rings alludes to the possibility of forming a stable point defect consisting of triangle or rhombus as is pointed out in Figure 13. Various indications for the existence of such defects were found. The most compelling one is what appears

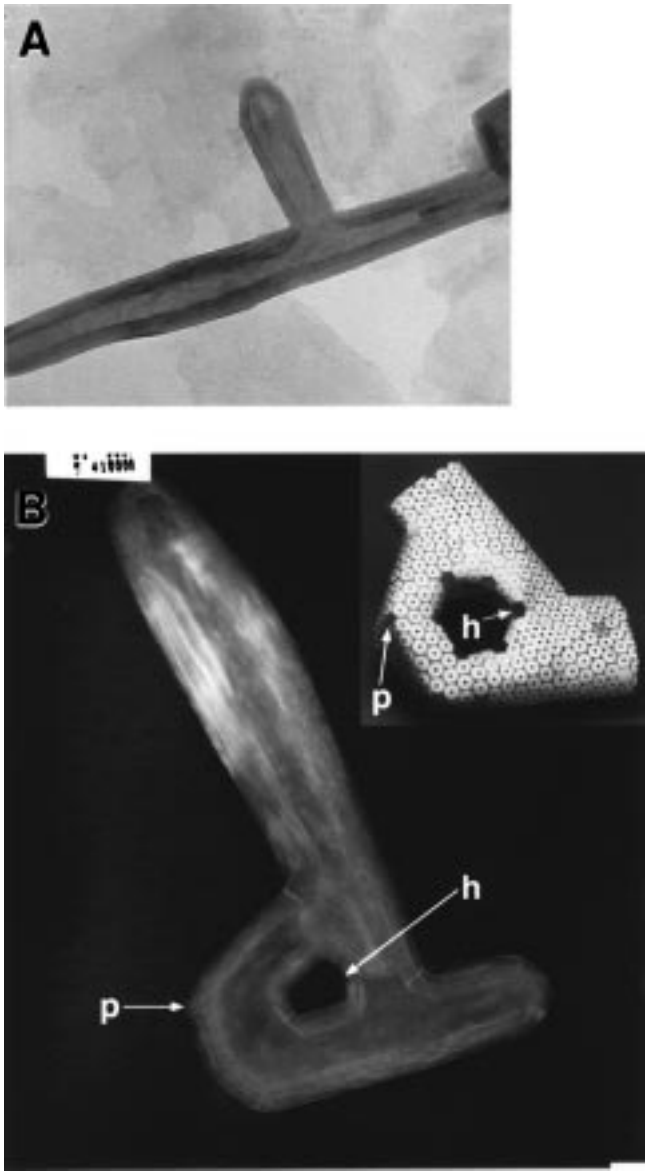

Figure 11. A typical hollow closed MoS_2 nanoparticle with a T-bar shape (A) and closed torous (B). A schematic model of the torus is included. The putative positions of the heptagons (h) and pentagons (p) are presented. These IF structures exhibit negative curvature.

to be a projection of a nested WS_2 "buckytetraheder", with a triangular defect at each of its 4 vertexes (Figure 13). Furthermore, a projection of a fullerene-like particle with right-angle corner consisting of a rhombus in one of its vertexes is shown in this figure too. A nonperfect "buckycube" was observed as well. Recently, a number of reports demonstrated the liklihood of the existence of four-membered rings in the apexes of BN cage structures and nanotubes.[39] Such point defects were not observed in carbon fullerenes, most likely because the sp^2 bonding of carbon atoms in graphite is not favorable for such topological elements. These examples and others illustrate the influence of the lattice structure of the layered compound on the topology of the IF structures.

III. Synthesis of IF Structures

1. Prelude. Various strategies were developed or adopted for the synthesis of hollow closed structures

Figure 12. Two entangled spiral WS_2 nanotubes (bundle of 2 coils).[38]

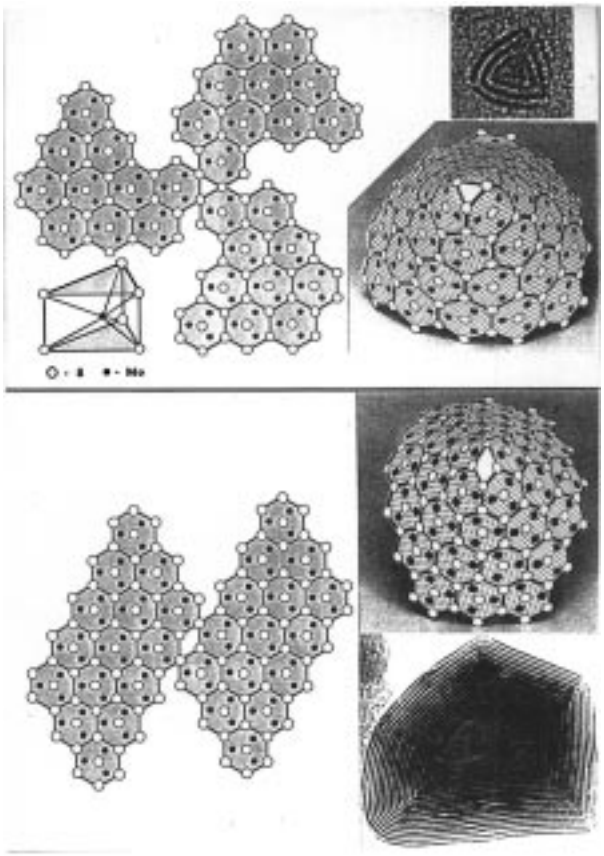

Figure 13. Illustration of possible point defects which exist in the vertexes of IF−MoS_2: (A) triangular point defect; (B) rhombohedral point defect. The TEM images demonstrate IF structures that are likely to contain such point defects. Distance between each two fringes is $c/2 = 0.62$ nm.

from layered compounds. One can distinguish between two kinds of procedures: (a) violent synthetic procedures that occur far from equilibrium, and (b) synthetic procedures that are maintained in close proximity to the domain of equilibrium conditions. The products of the reaction belonging to the first category must be purified aposteriori, which makes the scaleup of such a procedure very tedious and hence costly. On the other hand, the reaction parameters are controllable in the case of the second category, which entails high yields and selectivity for the product.

2. Far from Equilibrium Synthesis of IF Nanoparticles. The popular arc-discharge technique belongs in the first category. It has been used extensively in the past for the synthesis of fullerenes, Met-Cars,[26] nanotubes,[23a,24] endohedral fullerenes,[40] encapsulated nanotubes,[41] and nested fullerenes (onions).[42] Recently, the arc-discharge technique has been extended for the synthesis of composite carbon−BN−carbon nanotubes that could be useful for the fabrication of nanodiodes[43] and for the large scale synthesis of single-wall carbon nanotubes.[44] These latest accomplishments demonstrate the uniqueness of this technique for the synthesis of fullerene-related materials. Detonative reactions are another synthetic approach that belongs in this category and have been used in the past to synthesize, for example, diamond nanocrystallites.[45] Another synthetic strategy that belongs in this category is the self-propagating high temperature synthesis (SHS), which is a self-ignited combustion reaction. This method has been intensively studied for the preparation of, for example, ceramic powders.[46] In general, these techniques are not very selective and they afford a mixture of the products from which the most interesting ones must be isolated in a long and tedious procedure. However, they are able to produce metastable phases of species that are otherwise difficult to synthesize.

Another synthetic strategy that has been successfully used for the preparation of IF−MoS_2 structures is electron beam irradiation of MoS_2 crystals.[47] Beam-induced synthesis of nested carbon fullerenes and their modification were previously reported.[48,49]

Cluster synthesis by the laser ablation technique, which was realized first by Smalley and co-workers,[50] can be considered to belong in this category, too. The hot plasma produced by the incident laser beam elicits the growths of incipient nuclei. Subsequent expansion through a nozzle leads to a rapid quench (10^9 deg/s) during which the clusters develop into their final topology. The mass selectivity of the clusters obtained by the laser ablation technique cannot be attained by any other technique, in general.[50] Copious amounts of single-wall carbon nanotubes of small diameter were obtained by the laser ablation technique.[51] In a recent experiment, laser ablation was used to vaporize molybdenum oxide powder, which was subsequently reacted with H_2S in the presence of a reducing atmosphere. IF−MoS_2 including MoS_2 nanotubes were obtained.[52] The synthetic methodology used in this experiment is not very different from the gas-phase reaction that was previously reported.[53] With more time and effort, this technique is likely to become the major tool for the synthesis of mass-selective IF−MoS_2 of a precise number of atoms/cluster. This step is a prerequisite for the determination of IF−MoS_2 structures.

3. Synthesis of IF-MS_2 from a-MS_3 Nanoparticles. To locate the window of conditions most appropriate for the synthesis of IF, one must consider the binary phase diagram of the metal−chalcogen system near the composition of the layered structure. A demonstration of this idea is presented in the phase diagram of the W−S system, illustrated in Figure 14. Presumably, the IF phase can be obtained on the phase

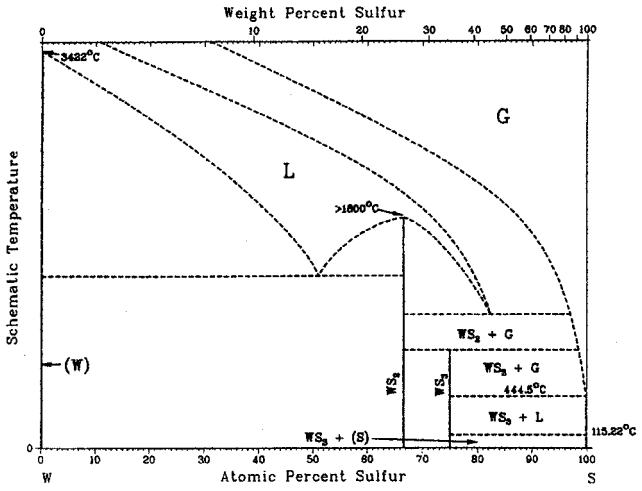

Figure 14. Phase diagram of the W−S system. The existence zone of the IF phase is at the phase boundary between the amorphous a-WS_3 and the crystalline 2H−WS_2 phases.

boundary between the amorphous WS_3 precursor and the crystalline 2H−WS_2 phase. The loss of sulfur from amorphous WS_3 (a-MS_3) nanoparticles triggers the nucleation of WS_2 nanocrystallites. If the coalescence of a-MS_3 can be avoided during crystallization, the isolated nanonuclei cannot grow into large crystallites at once, and hence they transform first into fullerene-like nanoparticles. Once these particles grow beyond 200 nm, for example, they become unstable and 2H−WS_2 platelets are preferred. This synthetic strategy has been demonstrated in a few experimental procedures.[53a]

In early experiments,[27] thin films (<20 nm) of tungsten were deposited on a quartz substrate, using e-beam evaporation. Such films are partially discontinuous and they also consist of isolated tungsten nanoparticles. The films were annealed in sulfur under reduced pressure. The product was examined by transmission electron microscope at various intervals of time. While heating under excess sulfur atmosphere, the oxide was gradually converted into a-WS_3 according to reaction 1. Further heating to ~850 °C led to the loss of one S atom and crystallization of the nanoparticles into the by-now characteristic IF−WS_2 structures (eq 2), as anticipated from the W−S phase diagram (Figure 14).[29c]

$$MO_{3-X}(g) + 3H_2S(g) \rightarrow MS_3(s) + (3 - X)H_2O(g) + XH_2(g) \quad (1)$$

$$MS_3(s) \rightarrow MS_2(s) + S(g) \qquad (M = W, Mo) \quad (2)$$

Because the phase boundary between amorphous WS_3 and crystalline 2H−WS_2 extends down to room temperature (Figure 14),[29c] one would expect to see spontaneous IF formation from WS_3 nanoparticles even at ambient conditions. Indeed, WS_3 samples that were left at room temperature and inspected from time to time started to show "hot spots" after ~1 year. The "hot spots" slowly crystallized, and new "hot spots" appeared throughout the sample with time. After 2 years, a few of them exhibited developed characteristic IF morphology.[29a] This process went on and many new IF were formed after 3 years from the time they were first put in the drawer. Facilitation of the sulfur abstraction from WS_3 by reaction with the ambient oxygen is not unlikely and is discussed later. The IF that were prepared at elevated temperatures and kept in the drawer did not show any structural evolution after a few years time and are therefore considered to be (meta)stable at room temperature, "indefinitely".

Although there is some disagreement concerning the occurrence of an amorphous MoS_3 (a-MoS_3) phase, a few reports indicated that this is the dominant phase in the Mo−S phase diagram at low temperatures and excess sulfur regime.[54] On elevating the reaction temperature, the 2H−MoS_2 polytype predominates. This situation is again favorable for the IF−MoS_2 formation from a-MoS_3 nanoparticles.

Modification of materials by pulse from a scanning tunneling microscopy (STM) tip were published.[55,56] To take advantage of the unique capabilities of the STM for synthesis, imaging, and analysis of IF nanoparticles, the following strategy was adopted. First, an a-MoS_3 film was electrochemically deposited on a gold substrate from a bath of 0.1 M ammonium thiomolybdate and 0.05 M Na_2SO_4 dissolved in an aqueous solution at pH 5 and a bias of 0.23 V versus saturated calomel electrode (SCE). The film consisted of two typical domains: one containing nanoparticles of 20−40 nm and a continuous film in the second part.

In the next step, an ambient STM with a Pt/Ir tip was used to image the surface and to induce crystallization of the amorphous film. Pulses ranging between 4 and 9 V (tip positive) were applied to induce crystallization of the amorphous nanoparticles, while the tip was positioned a few angstroms above the sample. The duration of the pulses varied from 10 to 1000 ms. During the pulse, the feedback loop was disengaged and a sample-hold-loop fixed the tip in its position. After the pulse was applied, the feedback system was reactivated and the scanning was resumed. Usually a few series of scan/pulse/scan routines were applied for a predefined area of ~50 × 50 nm^2. Incidentally, the a-MoS_3 nanoparticles are insulating and therefore they could not be resolved by the STM. Following the electrical pulse, typically 20 nm round and oblate-shape objects were identified by the STM. Using careful transfer procedure, both the a-MoS_3 and the crystallized nanoparticles could be easily resolved. In particular, the crystallized nanoparticles consisted of IF−MoS_2 shell and a-MoS_3 core, which was also confirmed by selected area energy-dispersive X-ray analysis (EDS). Particles smaller than, e.g. 15 nm, were fully converted into IF−MoS_2 with a hollow hole in the center.

Contrary to this behavior, a completely different mode of crystallization was observed for areas that were covered by a continuous thin film of a-MoS_3. Small 2H−MoS_2 platelets, which were embedded in the amorphous matrix, were formed as a result of the electrical pulse. The size of the crystalline domain is rather small (2−3 nm thick) in this case. The dissipation of thermal energy, deposited by the electrical pulse in the continuous Mo−S film, was probably very fast and hence the energy density was below the required threshold for sulfur abstraction and crystallization of the material.

The STM tip was also used for measurement of the tunneling current versus bias ($I-V$ curves). Prior to the application of the electrical pulses, an Ohmic behavior

was observed for the film. The $I-V$ curve that was measured while the tip was fixed above a crystallized nanoparticle exhibited a typical semiconductor-like behavior with a statistically averaged band gap of -1.1 eV (± 0.05 eV). The value of the band gap is similar to the (indirect) gap of the bulk (2H) material and was confirmed by direct optical measurements.[57] In fact, the shape of the $I-V$ curve, which changed from a metallic-like behavior to a semiconductor-like behavior, was another criteria used to judge the success of a pulse experiment.

The main mechanisms proposed for the process are field emission of electrons and atoms, deposition of thermal energy,[55] and vibrational excitation of surface atoms.[56] Alternatively, the reaction can be initiated by pulse-induced cleavage of oxygen and water molecules and formation of O· and OH· radicals. In the absence of data for the heat conductivity and heat capacity of MoS_3, the temperature rise cannot be calculated. Rough estimates for the temperature rise in amorphous metals under a similar pulse were as high as 1000 °C.[55]

To crystallize, each MoS_3 molecule in the nanoparticle must first lose one sulfur atom: $MoS_3 \rightarrow MoS_2 + S$ ($\Delta G^0 = -6.2$ kcal/mol[58]). This reaction is well documented in the literature. Because the reaction is carried out in ambient conditions, an alternative pathway involving sulfur abstraction by oxygen is possible:

$$MoS_3 + O_2 \rightarrow MoS_2 + SO_2\uparrow \qquad (\Delta G^0 = -77.6 \text{ kcal/mol}^{58}) \quad (3)$$

and

$$MoS_3 + {}^3/_2O_2 \rightarrow MoS_2 + SO_3\uparrow \qquad (\Delta G^0 = -94 \text{ kcal/mol}^{58}) \quad (4)$$

Although all processes are exothermic, the oxygen-induced reactions are appreciably more favorable, and the evolution of gaseous SO_2 (SO_3) drives the reaction to completion. However, the latter reactions might be kinetically hindered by shortage of oxygen, particularly for the crystallization of the inner MoS_2 layers.

The outermost layers of the fullerene-like nanoparticles are always complete. Also, the size and morphology of the fullerene-like nanoparticles do not seem to be influenced by the duration of the STM pulse. These facts indicate that the reaction starts at some point on the outer surface of the amorphous MoS_3 nanoparticle and is only terminated when the MoS_2 layers enveloping the surface are completed. These observations could possibly suggest a self-sustained, self-extinguishing mechanism that is reminiscent of the metathesis reactions between alkali sulfide and molybdenum (tungsten) halides.[59] Although the exothermicity of the metathesis reactions is appreciably larger, the present reaction produces heat in constricted domains of 15−40 nm. The heat cannot be effectively dissipated to the gold substrate, because of the small contact area between the spherical nanoparticle and the flat gold substrate film. Radiative emission to the ambient atmosphere is also rather slow. Therefore, the energy density that is released during the electrical pulse is probably higher than in the case of the metathesis reaction, and the reaction can therefore be self-sustaining. The local heating of the nanoparticle also provides the necessary energy to form the point defects, which are responsible for the bending of the otherwise flat surface of the hexagonal network.[18,26,59] Once the fullerene-like shell is completed, the reaction is switched off automatically. The threshold bias of 4 V is required for the initial abstraction of sulfur atoms through one of the aforementioned mechanisms. These atoms may remain on the STM tip surface and induce current instability, which is often observed after the pulse.

On the other hand the crystallization of the continuous film is interrupted very shortly after the pulse, and the domain size of the 2H-polytype nanocrystallites is very small (~2−3 nm) in this case, which suggests that the local heating of this sample due to the electrical pulse is confined to a very small domain and excludes a self-sustained reaction here. Most of the heat is shunted through the gold film, which serves as a substrate for the Mo−S film. The large contact area between these two films facilitates the heat transfer across the interface. These arguments indicate that the slow dissipation of electrical (thermal) energy from the amorphous nanoparticle leads to a very strong local heating of the nanoparticle. This effect is responsible for the thermally activated abstraction of sulfur from the compound.

In conclusion, very short electrical pulses from an STM tip were applied to amorphous MoS_3 nanoparticles and induced fast crystallization of an amorphous precursor into fullerene-like MoS_2 particles in ambient conditions. A mechanism for this unique process has been proposed. A Schottky-like junction between the fullerene-like MoS_2 nanoparticle and the supporting gold film has been established and is currently being investigated.

4. IF-MS_2 Synthesis from MO_3. Molybdenum oxide is volatile under reducing conditions >700 °C, and hence a gas-phase reaction was adopted for the synthesis of IF−MoS_2.[53,60] Typically, a 30-mg portion of MoO_3 powder (>99% pure) is heated (>800 °C) and is slowly reduced to MoO_{3-x} by a stream of forming gas (typically 5%H_2/95%N_2). The suboxide sublimes and effuses out of a nozzle where it crosses a stream of H_2S gas mixed with a forming gas. The reaction products are collected on a quartz scepter, which is positioned 3 cm away from the crossing point of the two gas streams and is maintained at the same temperature (>800 °C). The collected nanoparticles are progressively converted into nested IF polyhedra within ~30 min of firing time. The average size of the oxide nanoparticle and the ensuing IF−MoS_2 increases with temperature. It was found that at >900 °C, platelets with the 2H−MoS_2 structure abound and become the sole product at >950 °C.

Because WO_3 is not volatile at these temperatures, the solid (WO_3)−gas ($H_2S + H_2$) reaction was preferred in this case.[61] The starting material for the synthesis of IF−WS_2 is a WO_3 powder (>99% pure), with particle sizes smaller than ~150 nm. To avoid agglomeration and fusion of the heated nanoparticles, the powder was carefully dispersed on the entire floor of the reactor boat, resulting in a complete exposure of the nanoparticle surface to the reacting gas. In contrast to IF nanoparticles, platelets of 2H−WS_2 were predominantly obtained under the following experimental conditions: packing of the powder was too compact; oxide particles

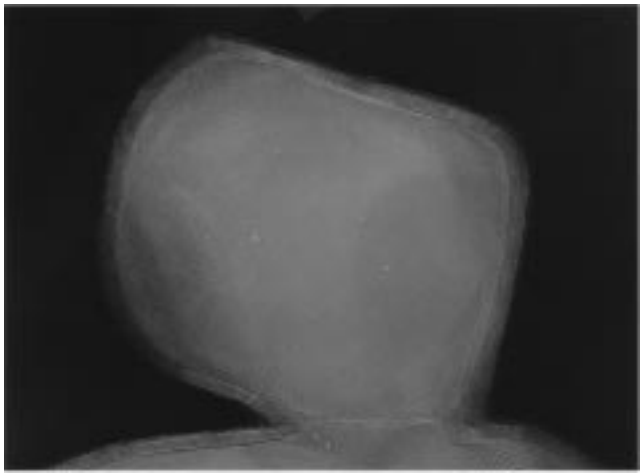

Figure 15. IF−SnS_2 structure obtained by controlled sulfidization of a SnO_2 nanoparticle. The distance between each two fringes is 0.59 nm.

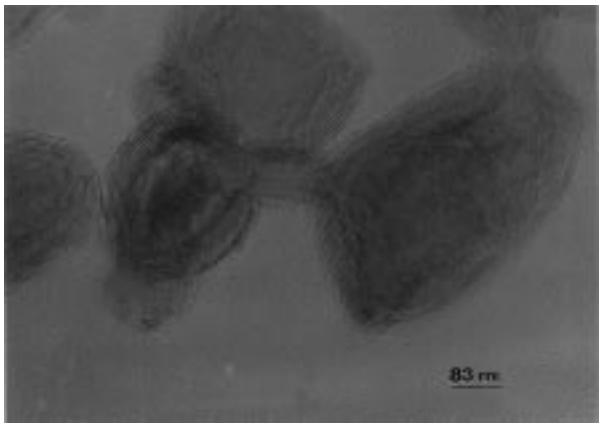

Figure 16. IF−VS_2 structure obtained through reduction/sulfidization reaction of Na-doped V_2O_5 nanoparticles, which were synthesized by a modified evaporation apparatus.[62]

with sizes >0.2 μm were used; and reaction temperature exceeded 900 °C.

A similar procedure has been employed for the synthesis of IF structures from different layered metal dichalcogenides and metal chalcogenides.[62] Figure 15 shows a TEM image of a closed SnS_2 (CdI_2 structure) nanoparticle with an oxide core. To synthesize this kind of nanoparticle, tin oxide powder consisting of particles <150 nm were sulfidized in a reducing atmosphere. Similar procedures were employed for the synthesis of IF−VS_2 particles (Figure 16), etc.[62] A novel method for the intercalation of the IF materials, by first doping oxide nanoparticles with alkali metal atoms and subsequent sulfidization of the oxide nanoparticles was demonstrated as well.[62] Presumably, the formation of stable IF−VS_2 could not possibly occur without the Na intercalation that leads to partial charge transfer and thereby stabilizes the layered structure of this compound.[63]

A novel growth mode for MoS_2 nanotubes has been recently demonstrated by Zelenski and Dorhout.[64] In this method, $(NH_4)_2MoS_4$ and $(NH_4)_2Mo_3S_{13}$ solutions were permeated through the empty voids of a nanoporous aluminum oxide membrane. Thermal treatment of the sample led to a complete decomposition of the thiomolybdates. The walls of the aluminum oxide pores

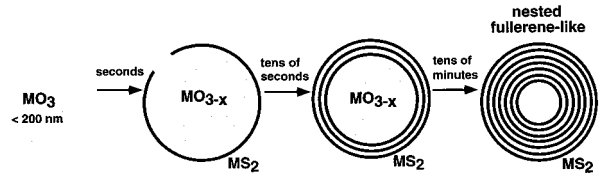

Figure 17. Schematic representation of the growth model of the inorganic fullerene-like nested polyhedra from oxide nanoparticles.

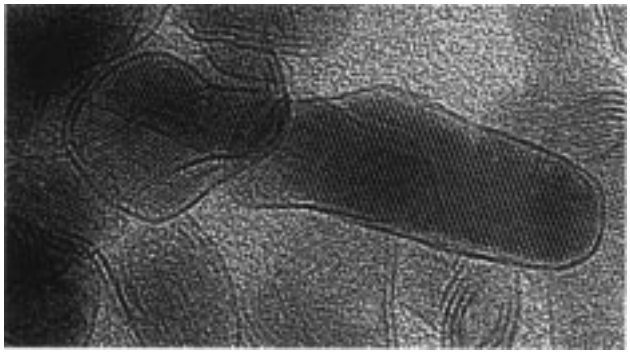

Figure 18. Demonstration of the initial stage in the growth process of the IF−WS_2 nanoparticle. A single layer of WS_2 encases the oxide nanocrystallite and "isolates" it from the surrounding nanoparticles.

served in this case as a template for the growth of MoS_2 nanotubes. Subsequent soaking in NaOH solution led to a selective dissolution of the membrane. It is likely that the nonperfect structure of the nanotubes was influenced by the nonregular shape of the pores in the host membrane and also by the relatively low annealing temperature (450 °C).

The growth mechanism of the IF particles from oxide precursors and $H_2S/H_2/N_2$ gas mixture has been discussed in detail and will be only briefly presented here. Figure 17 is a cartoon of the proposed growth model for quasispherical nested nanoparticles and nanotubes. In the first instant of the reaction, the oxide nanoparticle reacts with H_2S gas, which leads to the growth of a complete sulfide shell consisting of one or two MS_2 atomic layers engulfing the entire oxide nanoparticle, as shown in the high-resolution TEM (HRTEM) micrograph of Figure 18. This sulfide shell isolates the nanoparticle from its nearest neighbors thereby prohibiting coalescence of the nanoparticles, which would lead to the formation of 2H-MS_2 platelets. Within a very short time (~1 min), hydrogen diffusion into the nanoparticles (and oxygen outdiffusion) leads to reduction of the oxide core and formation of crystallographic shear plans.

In the second stage of the reaction, which can last between 30 and 120 min and even more, sulfur diffuses slowly into the core and slowly converts the suboxide into sulfide, which becomes hollow at the end of the process. The rate-determining step in this process was attributed to the intercalation of sulfur in the topmost sulfide layers and its slow diffusion toward the growth front inside the nanoparticle. This process actually consists of two separate processes. The rapid radial diffusion of sulfur atoms inward through dislocation at the outer MS_2 layers and the slow diffusion of the sulfur atoms along the layers into the single-growth front of the sulfide. This process provides a continuous MS_2 shell that grows inward into the oxide core. Figure 19

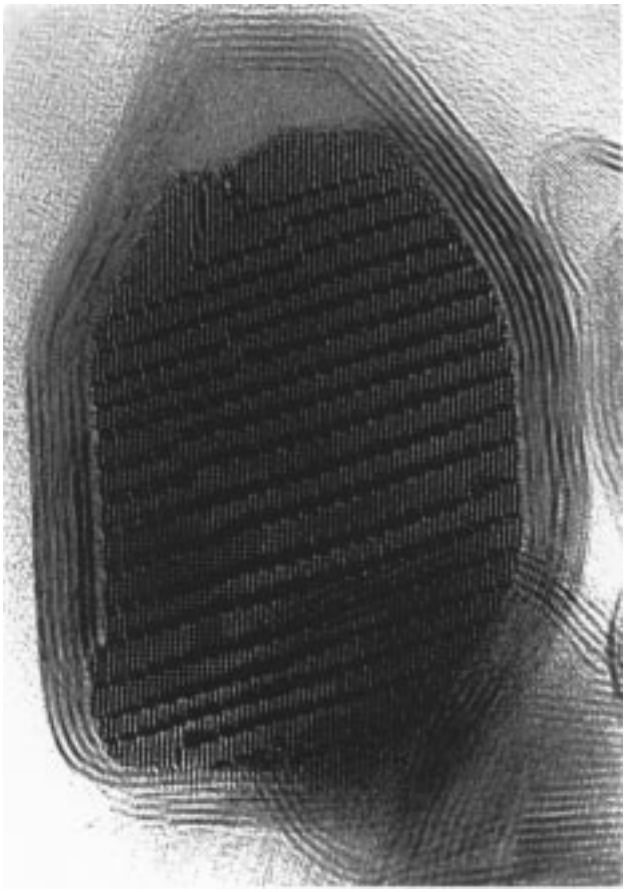

Figure 19. Large WO_{3-x} encapsulate with 18 $(103)_R$ Wadsley-type crystal shear planes interspersed in an ReO_3-type WO_3 sublattice (0.38 nm lattice fringes). Note the single growth front of the sulfide layer and the quasi-epitaxial matching between this growth front and the top (outer) sulfide layer.

presents an HRTEM micrograph demonstrating an intermediate stage in this process in a single nanoparticle. The sulfide growth front as well as the crystallographic shear plans of the core oxide are clearly observed in this image.

It is clear from the discussion just presented that the first instant of growth of the sulfide on the surface of the oxide nanoparticle determines whether the usual 2H platelet will be formed or a closed incipient sulfide shell, which protects the oxide nanoparticle from coalescing with neighboring nanoparticles and furnish the conditions for IF growth, prevails. In a recent work,[65] a detailed study of this primary process has been undertaken and a model involving elementary physicochemical steps has been proposed. It was found, that for the conditions used in our reactor, the rate of the sulfidization reaction is favorable at low temperatures (<600 °C), whereas the rate of the reduction process prevails at temperatures >800 °C. Furthermore, the IF growth occured at the intermediate temperature interval where the rates of the two reactions are comparable. To account for the wealth of experimental data, a growth model was proposed. According to this model a *synergy between the reduction and sulfidization* processes, which occurs in a rather narrow window of the experimental parameters, leads to the formation of the first 1−2 closed sulfide layers.

The microscopic (atomistic) view of this growth model can be realized through the schematics of Figure 20. The

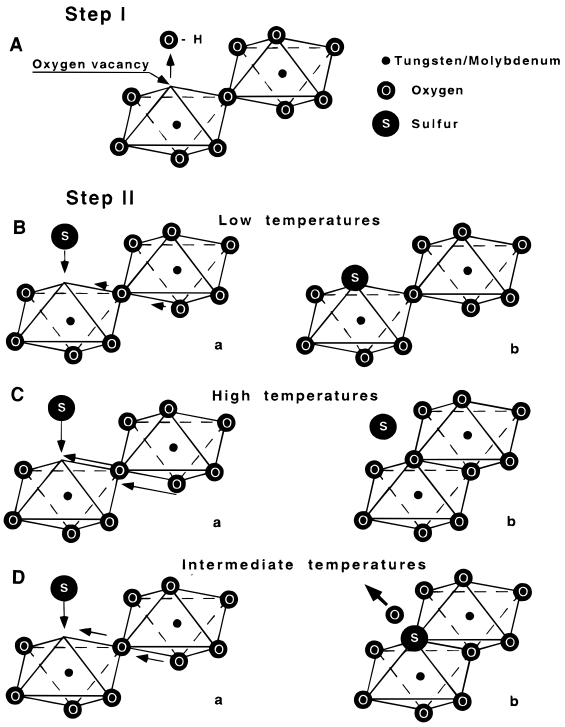

Figure 20. Schematic drawing of the various processes that occur during the sulfidization of the metal-oxide particles. The oxide precursor is represented as two octahedra connected via a corner oxygen atom. (A) Preliminary step: oxygen atom leaves the octahedron and an oxygen vacancy is thus formed. The three possible subsequent steps are shown in B−D. (B) Sulfidization of the oxide at low temperatures. The rates of the processes are represented schematically by the size of the arrows. Thus, the rate of the shear process is slow compared with sulfur trapping by the vacancy and, consequently, sulfur trapping predominates. (C) Sulfidization of the oxide at high temperatures. The rate of both the shear process and sulfur trapping increase with temperature, however, the former one predominates. Therefore, shear (reduction of the oxide) prevails at these temperatures. (D) At intermediate temperatures (600−850 °C), the rate of both processes are of the same order of magnitude and the sulfidization and shear appear at the same time, leading to the formation of the superficial sulfide layer engulfing the oxide nanoparticle: a, representation of the situation prior to the process; b, after the process has been completed.

creation of oxygen vacancies on the surface of the oxide particles by hydrogen is most probably the first step in the entire (reduction−sulfidization) process (Figure 20A). Hence, two competing events follow: the first one is vacancy annihilation by the shear process; the second event is sulfur occupation of the oxygen vacancy site. As already noted, sulfur occupation of the vacancy sites is more rapid than vacancy annihilation by shear process (reduction) at low temperatures (Figure 20B), whereas the reduction process prevails at high temperatures (Figure 20C). In intermediate temperatures (600−850 °C), the rate of the two processes is equivalent (for a given set of experimental parameters, this range is much narrower). During the shear of an octahedron, the oxygen atom, which hops from one corner to a neighboring vacancy, has to break its chemical bond to its nearest metal neighbor and consequently it is more prone to a chemical reaction or substitution at this instant of time. When the probability of oxygen leaving (reduction of oxide) equals the probability of the sulfur occupation of the oxygen vacancy site, the kinetic rate

of the oxygen substitution by sulfur is the largest (Figure 20D). On the other hand, the sulfur−oxygen exchange accelerates the autocatalytic reduction effect.[66] Thus, a synergy between the autocatalytic reduction and oxygen−sulfur exchange prevails when the rates of the two processes are equivalent.

From the microscopic viewpoint there is a significant difference between the low- and high-temperature processes and that in the intermediate temperatures. In the low- and high-temperature processes (Figures 20B and C) no oxygen atom is abstracted. In contrast to that, one oxygen atom is released when the two process (shear/sulfidization) occur in a concerted manner (Figure 20D). Moreover, this situation leads to the bonding of the captured sulfur atom to two neighboring metal atoms, which is opposite to the situation at low temperatures. Subsequent abstraction of oxygen atoms, shear, and concomitant sulfur atom capturing from the gas phase promotes the growth of the MS_2 surface layer encasing the oxide nanoparticle. It is therefore believed that the *synergy between the reduction and sulfidization processes provides the conditions for IF formation in a certain range of experimental parameters*. It should be noted, that the growth rate of the sulfide layer on the surface of the large oxide particles is not sufficient to wrap the entire surface, whereas reduction of the oxide takes place and they all break-up into smaller crystallites, which precludes IF formation from large oxide particles.

The formation of a *thin sulfide skin controls the size of the fullerene-like nanoparticle*. Once the size and shape are fixed, further transformation of the oxide into sulfide takes place internally. The growth of the next inner sulfide layers does not change the morphology of the outer layers substantially. However, it was suggested[53b] and later confirmed experimentally[61] that initially the thin sulfide layers are evenly folded, while thickened sulfide mulitlayers exhibit more polyhedral topology (i.e., the point defects responsible for the folding form order arrays across the sulfide layers; e.g. compare Figures 18 and 19).

Synthesis of IF−WSe_2[29b] also shows good agreement with the present model. The cross point between the reduction and selenization processes is observed at lower temperatures (typically 760 °C) compared with 840 °C for IF−sulfide formation. Higher reaction temperatures yielded platelets (2H) of the respective selenides. Hence, the synergy between selenization and reduction, which is a prerequisite for the IF formation, occurs at lower temperatures than that of the respective sulfide. This tendency is confirmed by the available experimental data.[29b]

IV. The Structure of MoS_2 (WS_2) Nanotubes

1. Working Hypotheses. To develop a structural model for the nanotubes, the following hypotheses are used:

1. The strength of the Mo−S chemical bonds entails fixed Mo−S and Mo−Mo distances, which are not affected by the weak curvature of the layer. Contrarily, the S−S interlayer distances, and to some extent, the distance between two sulfur atoms within a sulfur layer, are susceptible to distortion during folding of the layers. Thus, it is likely that, although the S−S distance in the upper sulfur layer of MoS_2 shell increases, the S−S distance in the lower sulfur layer of the same shell decreases. The Mo−Mo distance within a layer corresponds to the lattice parameter "*a*" (a = 3.16 Å). Experimentally, it was observed that the *c*/2 parameter of the lattice (6.15 Å) in the IF−WS_2 increases by 2% *vis-a-vis* the single crystal.

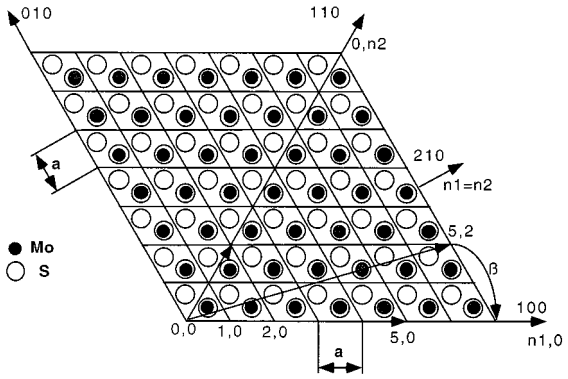

Figure 21. Schematic representation of nanotube formation by folding single MoS_2 plane.

2. Consider a nanotube with a cross section with radius R. The length of the arc corresponding to an angle α is $2\pi R\alpha/2\pi = R\alpha$. The corresponding length of a chord that connects the two extreme points of the arc (i.e., it makes the same angle α) is $2R\sin(\alpha/2)$. For R = 20 Å and a = 3.16 Å, the difference between the lengths of the arc and the chord that connect two Mo atoms is 0.1%, which is less than the experimental error in determining these distances. Hence, it is legitimate to interchange the chord and the arc for nanotubes of a radius 20 Å and higher.

3. Let the S−Mo−S layers have the radii (R − 1.6 Å)−R−(R + 1.6 Å), respectively. The number of atoms ($N = 2\pi R/a$) is the same for all three layers.

4. A defect is generated when the stress between two neighboring sulfur atoms during folding is larger than the energy of the Mo−S chemical bond. The distance between the Mo and S layers within the shell is ΔR = 1.6 Å. The smallest observed radius for a MoS_2 nanotube was R = 30 Å.[67] From these considerations, the maximum deformation of the layer can be $\Delta a/a = \Delta R/R$ = 5%.

5. The 2H symmetry of the MoS_2 lattice is locally preserved, which is indicated by XRD measurements.

2. Correlation of Crystallographic Directions and Helicity Angles. *1. The Selection of the Integers n_1 and n_2.* The integers n_1 and n_2 (Figure 21) are defined in complete analogy to the convention used for carbon nanotubes;[68] that is, n_1 and n_2 are the number of Mo atoms along the [100] and [110] axes, respectively. The vector [n_1,n_2] points to the Mo atom, which coincides with the Mo atom in the origin of the system of axes by folding a sheet of one MoS_2 layer into a tube. The length of the vector [n_1,n_2] is $2\pi R$; it forms a circle that is perpendicular to the tube axis. The chirality of the nanotube is fully specified by these two indices.

2. Correlation between n_1, n_2, Diameter (d), and β, the Helicity Angle. Let β, the helicity angle, be defined such that it is equal to zero when the vector [100] is directed along the cross section that is perpendicular to the tube axis. Therefore [120] is the tube axis in this

Table 1. The Relation between the Chirality (Helicity) Angle and the Lattice Parameters n_1 and n_2 of Two Neighboring Atomic Layers in MoS_2 Nanotube

Δn_2	β, helicity angle (deg)	Δn_1	Δn_2	β, helicity angle (deg)	Δn_1
0	0	12.2	4	16.46	9.7
1	4.06	11.7	5	20.74	9
2	8.14	11.1	6	25.15	8.1
3	12.27	10.4	7	29.72	7.1

case, and the length of the perimeter of the cross section is $n_1 a$. In this case, n_2 is zero.

For a given angle β, n_1 and n_2 are determined from the following relationships

$$\tan \beta = n_2\sqrt{3}/(2n_1 + n_2) \quad (5)$$

$$n_1 = (\cos \beta - \sin \beta/\sqrt{3})\pi(d/a) \quad (6)$$

$$n_2 = 2\pi d \sin \beta/a\sqrt{3} \quad (7)$$

$$\pi(d/a) = \sqrt{(n_1^2 + n_2^2 + n_1 n_2)} \quad (8)$$

For $n_1 > n_2$, the chirality angle is $\beta < 30°$ and the chirality is left-handed. The maximum chirality angle of the nanotube is $\beta = 30°$ ($n_1 = n_2$). In this case, the vector $[n_1,n_2]$ is pointing along the [210] direction (Figure 21). When β is $>30°$ ($n_2 > n_1$), a new chirality angle $\beta_1 = 60 - \beta$ can be defined. It can be shown that by interchanging the role of the two indices, β_1 becomes completely equivalent to another chirality angle $\beta' < 30°$, which is right-handed and is defined with respect to a new crystallographic axis $[\bar{1}\bar{1}0]$ with $n_1 > n_2$.

3. Estimation of Δn_1, Δn_2, and the Helicity Angle (β) for a Multilayer Monohelical MoS_2 Nanotube. In this section, the relationship between the structural parameters of two neighboring MoS_2 layers are determined for a multilayer nanotube. Δn_1 and Δn_2 are the variations in the indices n_1 and n_2, respectively, between the two neighboring MoS_2 layers. The distance between the two layers is given by: $d_2 - d_1 = \Delta d = c = 12.3$ Å, where d_1 and d_2 are the diameters of the 2-folded layers, and β is the helicity angle of the two nanotubes.

From eq 7,

$$\beta = \sin^{-1}(\Delta n 2a\sqrt{3}/2c\pi) \quad (7a)$$

and from eq 6

$$\Delta n_1 = (\cos \beta - \sin \beta/\sqrt{3})c\pi/_a \quad (6a)$$

where $a = 3.16$ Å.

Table 1 summarizes a few calculated values of the chirality angle and the indices n_1 and n_2 of two neighboring atomic shells in the MoS_2 nanotube. Analysis of the chirality angle of multilayer MoS_2 nanotubes was carried-out previously.[67] The typical helicity angles reported were 13, 20, and 29°, which agree well with some of the calculated values in Table 1.

4. The Folded Carpet (Scroll-Shaped) Model. One possible way to explain the growth mode of MoS_2 nanotubes would be the folded carpet model, in which an MoS_2 shell grows and folds continuously in a spiral mode on top of the underlying MoS_2 shell, which was formed in the previous step. A similar model was proposed for the growth of carbon whiskers[69] and

Figure 22. TEM image of a MoS_2 nanotube with arrested growth of a few sulfide layers inside the core of the nanotube that is observed on both sides of the nanotube.

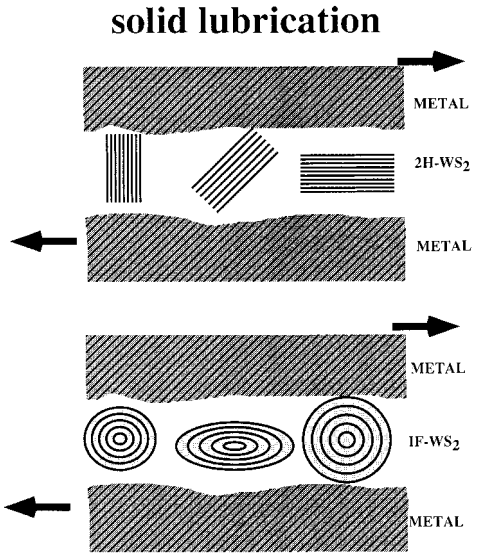

Figure 23. Schematic representation of the action of solid lubricant particles between two reciprocating metal surfaces: (A) 2H−WS_2 platelets; (B) quasispherical IF−WS_2 nanoparticles.

nanotubes.[70] The number of MoS_2 molecules in the layer varies with the radius of the nanotube, which excludes full comensuration.[53a,71−73] Nonetheless, it was found that the 2H structure is locally preserved. Thus, it is impossible for a single layer of MoS_2 to grow in the folded carpet mode because, in this case, the top layer will be in antiphase *vis-a-vis* the underlying shell (i.e., the sulfur atoms will be arranged in opposite direction to the one expected for a 2H polytype). If the two MoS_2 layers are coupled and grow together with a single growth front, they will be in phase with respect to the underlying layer, but coupled growth of two MoS_2 layers in a single growth front has not been observed. For example, it has been often observed that the growth of a single (and not double) MoS_2 (WS_2) layer is arrested either along the inner or outer perimeter of the nanotube (see Figure 22).

Furthermore, in the case of a chiral nanotube, the folded carpet model would entail a sudden discontinuation of a layer (fringe) on one side of the nanotube. By tilting the sample, the position of the discontinuity would vary continuously along the tube axis. Also, the nanotube would have unclosed caps at the two ends. Both assumptions are not validated by TEM analysis.

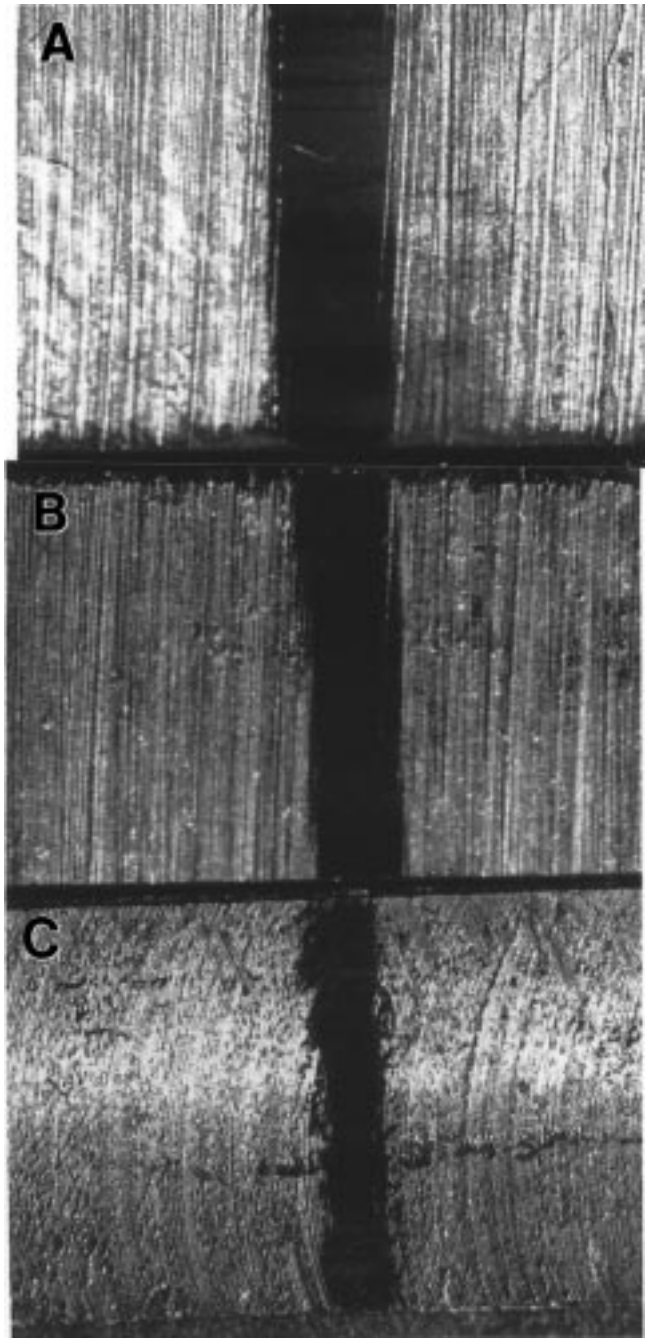

Figure 24. Results of the disc-block tribological test. The scar left on the flat block after the tests are compared for three solid lubricants mixed with lubrication fluid (5 wt %): (A) 2H−WS_2; (B) 2H−MoS_2; and (C) IF−WS_2. The superior protection of the IF−WS_2 against wear of the metal piece is clear. In this experiment, velocity of the disk was 0.22 m/s; load was 1800 N, and the experiment went for 6 h.

Therefore the folded carpet model does not seem to provide a correct picture of the growth mode of the presently synthesized nanotubes.

At present there is not enough data to support a definite growth model for the very long, quasiperfect MoS_2 nanotubes previously reported.[53a]

V. Applications

Of all, the currently most compelling application, for the fullerene-like materials is in the field of tribology, where 2H−MoS_2 platelets have already found substantial number of applications.[74,75] The main advantage of the fullerene-like nested particles would be their seamless structure, which inhibits the sticking and burnishing of the nanoparticles by the surfaces of the reciprocating metal pieces during action (see Figure 23). Furthermore, the quasispherical IF−WS_2 nanoparticles serve as effective spacers, prohibiting contact and wear of the asperities of the metal surfaces under heavy loads where fluids are usually squeezed out.[76] Extensive experimental evidence in support of this view has been recently gathered.[77] Figure 24 shows a comparison of the scar left on a flat metal block due to the contact with a rotating disk dipped in three different slurries containing 2H−WS_2 platelets (A), 2H−MoS_2 platelets (B), and IF−WS_2 (C) mixed with oil in 5% weight percent. The substantially reduced wear and the smallest friction coefficient affected by the IF−WS_2 offer concrete evidence in favor of using this new brand of nanomaterials as solid lubricants. Further progress in the synthesis of nanoparticles of smaller diameter (30 nm) and with more even spherical shape may lead to substantial additional improvements in the quality of these new solid lubricants.

VI. Conclusion

Synthesis of nanoparticles of layered compounds with a structure radically different from the bulk counterparts and related to carbon fullerenes and carbon nanotubes was demonstrated. The underlying principles for their formation and in particular their large-scale synthesis have only been recently realized. Using various synthetic methodologies, hollow nanoparticles from various layered metal chalcogenides were synthesized, which has also been recently realized through the works of others.[47,64,78] Numerous applications for such nanostructures can be envisaged. Recently, the superior tribological behavior of IF−WS_2 nanoparticles mixed in lubrications fluids has been demonstrated, which led to a widespread industrial interest in this product.

To elucidate the folding mechanism of such structures, mass-selected clusters with small number of MS_2 molecules must be prepared and their structure should be studied. Theoretical calculations should be forwarded to unravel the structural changes in the MS_2 layer during the formation of the cage structure and its influence on the electronic and other physical properties of the nanoclusters.

Acknowledgment. We are grateful to Drs. J. Slaon and J. L. Hutchison of Oxford University for the HRTEM micrographs shown in this paper and to Dr. L. Rapoport of the Center for Technological Education-Holon (Israel) for the tribological measurements. Financial support for this work was obtained from the following sources: NEDO (Japan); Minerva (Münich); Israel Science Foundation, Israeli Ministry of Science (Tashtiot).

References

(1) Pauling, L. *Proc. Nat. Acad. Sci.* **1930**, *16*, 578.

(2) (a) Kato, K.; Kawada, I.; Takahashi, T. *Acta Crystallogr.* **1977**, *B33*, 3437. (b) Guemas, L.; Rabu, P.; Meerschut, A.; Rouxel, J. *Mater. Res. Bull.* **1988**, *23*, 1061. (c) Wiegers, G. A.; Meerschut, A. *J. Alloys Comp.* **1992**, *178*, 351. (d) Suzuki, K.; Enoki, T.; Imaeda, K. *Solid State Comm.* **1991**, *78*, 73.

(3) Greenwood, N. N.; Earnshaw, A. *Chemistry of the Elements*; Pergamon: Oxford, 1990; pp 171−220.
(4) Mackay, A. L. *Acta Crystallogr.* **1962**, *15*, 916.
(5) Sadoc, J. F.; Dixmier, J.; Guinier, A. *J. Non-Cryst. Solids* **1973**, *12*, 76.
(6) Briant, C. L.; Burton, J. J. *Phys. Status Solidi B* **1978**, *85*, 393.
(7) Hoare, M. R. *Ann. N. Y. Acad. Sci.* **1976**, *279*, 186.
(8) Frank, F. C. *Proc. R. Soc. London, Ser. A* **1952**, *215*, 43.
(9) Winters, R. R.; Hammack, W. S. *Science* **1993**, *260*, 202.
(10) Ino, S.; Ogawa, S. *J. Phys. Soc. Jpn.* **1967**, *22*, 1365.
(11) Edwards, P. P. *Proc. Mater. Res. Soc. Symp. Chem. Processes Inorg. Mater.* Persans, P. P.; Bradley, J. S.; Chianelli, R. R.; Schmid, G., Eds.; **1992**, *272*, 311.
(12) Farges, J.; de Feraudy, M. F.; Raoult, B.; Torchet, G. *NATO ASI Ser., Ser. B: Physics* Jena, P.; Rao, B. K.; Khanna S. N., Eds.; **1986**, *158*, 15.
(13) (a) Martin, T. P.; Bergmann, T.; Göhlich, H.; Lange, T. *Chem. Phys. Lett.* **1991**, *176*, 343. (b) Martin, T. P. *Phys. Rep. Phys. Lett.* **1996**, *273*, 199−242.
(14) Echt, O.; Sattler, K.; Recknagel, E. *Phys. Rev. Lett.* **1981**, *47*, 1121.
(15) Raoult, B.; Farges, J.; De Feraudy, M. F.; Torchet, G. *Z. Physik D* **1989**, *12*, 85.
(16) Cleveland C. L.; Landman, U. *J. Chem. Phys.* **1991**, *94*, 7376.
(17) Yatsuya, S.; Uyeda, R.; Fukano, Y. *Jpn. J. Appl. Phys.* **1972**, *11*, 408.
(18) Hubert, H.; Devouard, B.; Garvie, L. A. J.; O'Keeffe, M.; Buseck, P. R.; Petuskey, W. T.; McMillan, P. F. *Nature* **1998**, *391*, 376.
(19) Kroto, H. W. *Nature* **1987**, *329*, 529.
(20) Iijima, S. *J. Cryst. Growth* **1980**, *50*, 675.
(21) Iijima, S. *Nature* **1991**, *354*, 56.
(22) (a) Iijima, S.; Ichihashi, T.; Ando, Y. *Nature* **1992**, *356*, 776. (b) Mackay, A. L.; Terrones, H. *Nature* **1991**, *352*, 762. (c) Dunlap, B. I. *Phys. Rev. B* **1992**, *46*, 1933.
(23) (a) Krätschmer, W. A.; Lamb, L. D.; Fostiropoulos, K.; Huffman, D. R. *Nature* **1990**, *347*, 354. (b) Guo, T.; Jin, C.; Smalley, R. E. *J. Phys. Chem.* **1991**, *95*, 4948.
(24) Ebbesen, T. W.; Ajayan, P. M. *Nature* **1992**, *358*, 220.
(25) (a) Guo, B. C.; Kerns, K. P.; Catleman, A. W. *Science* **1992**, *255*, 1411. (b) Guo, B. C.; Wei, S.; Purnell, J.; Buzza, S.; Catleman, A. W. *Science* **1992**, *256*, 515.
(26) Cartier, S. F.; Chen, Z. Y.; Walder, G. J.; Sleppy, C. R.; Catleman, A. W. *Science* **1993**, *260*, 195.
(27) Tenne, R.; Margulis, L.; Genut, M.; Hodes G. *Nature* **1992**, *360*, 444.
(28) Margulis, L.; Salitra, G.; Tenne, R.; Talianker, M. *Nature* **1993**, *365*, 113.
(29) (a) Hershfinkel, M.; Gheber, L. A.; Volterra, V.; Hutchison, J. L.; Margulis, L.; Tenne, R. *J. Am. Chem. Soc.* **1994**, *116*, 1914. (b) Tsirlina, T.; Feldman, Y.; Homyonfer, M.; Sloan, J.; Hutchison J. L.; Tenne, R. *Fullerene Sci. Tech.* **1998**, *6(1)*, 157. (c) Tenne, R. *Adv. Mater.* **1995**, *7*, 965.
(30) (a) Cohen, M. L. *Solid State Comm.* **1994**, *92*, 45. (b) Rubio, A.; Corkill, J. L.; Cohen, M. L. *Phys. Rev. B* **1994**, *49*, 5081. (c) Miyamoto, Y.; Rubio, A.; Louie, S. G.; Cohen, M. L. *Phys. Rev. B* **1994**, *50*, 18360.
(31) Kobayashi K.; Kurita, N. *Phys. Rev. Lett.* **1993**, *70*, 3542.
(32) (a) Stephan, O.; Ajayan, P. M.; Colliex, C.; Redlich, Ph.; Lambert, J. M.; Bernier, P.; Lefin, P. *Science* **1994**, *266*, 1683. (b) Weng-Sieh, Z.; Cherrey, K.; Chopra, N. G.; Blase, X.; Miyamoto, Y.; Rubio, A.; Cohen, M. L.; Louie, S. G.; Zettl, A.; Gronsky, R. *Phys. Rev. B* **1994**, *51*, 11229. (c) Romanian work in *Inorg. Chem.*
(33) (a) Jensen, F.; Toftlund, H. *Chem. Phys. Lett.* **1993**, *201*, 89. (b) Silaghi-Dumitrescu, I.; Heiduc, I.; Sowerby, D. B. *Inorg. Chem.* **1993**, *32*, 3755.
(34) Yakobson, B. I.; Smalley, R. E. *Am. Scientist* **1997**, *85*, 324.
(35) Iijima, S.; Ichihashi, T.; Ando, Y. *Nature* **1992**, *356*, 776.
(36) (a) Jones, D. E. H. *Nature* **1991**, *351*, 526. (b) Mackay, A. L.; Terrones, H. *Nature* **1991**, *352*, 762. (c) Iijima, S.; Ajayan, P. M.; Ichihashi, T. *Phys. Rev. Lett.* **1991**, *69*, 3100. (d) Vandervilt, D.; Tersoff, J. *Phys. Rev. Lett.* **1992**, *68*, 511. (e) Dunlap, B. I. *Phys. Rev. B* **1992**, *46*, 1933.
(37) Homyonfer, M.; Feldman, Y.; Margulis, L.; Tenne, R. *Fullerene Sci. Technol.* **1998**, *6(1)*, 59.
(38) Remskar, M.; Skraba, Z.; Regula, M.; Ballif, C.; Sanjinés, R.; Lévy, F. *Adv. Mater.* **1998**, *10*, 248.
(39) (a) Terrones, M.; Hsu, W. K.; Terrones, H.; Zhang, J. P.; Ramos, S.; Hare, J. P.; Castillo, R.; Prassides, K.; Cheetham, A. K.; Kroto, H. W.; Walton, D. R. M. *Chem. Phys. Lett.* **1996**, *259*, 568. (b) Loiseau, A.; Willaime, F.; Demoncy, N.; Hug, G.; Pascard, H. *Phys. Rev. Lett.* **1996**, *76*, 4737.
(40) Takata, M.; Umeda, B.; Nishibori, E.; Sakata, M.; Saito, Y.; Ohno, M.; Shinohara, H. *Nature* **1995**, *377*, 46.
(41) (a) Seraphin, S.; Zhou, D.; Jiao, J.; Withers, J. C.; Loutfy, R. *Nature* **1993**, *362*, 503. (b) Yosida, Y. *Appl. Phys. Lett.* **1994**, *64*, 3048. (c) Guerret-Piécourt, C.; Le Bouar, Y.; Loiseau, A.; Pascard, H. *Nature* **1994**, *372*, 761.
(42) (a) Tomita, M.; Saito, Y.; Hayashi, T. *Jpn. J. Appl. Phys., Part 2* **1993**, *32*, L280. (b) Hare, J. P.; Hsu, W. K.; Kroto, H. W.; Lappas, A.; Prassides, K.; Terrones, M.; Walton, D. R. M. *Chem. Mat.* **1996**, *8*, 6.
(43) Suenaga, K.; Colliex, C.; Demoncy, N.; Loiseau, A.; Pascard, H.; Willaime, F. *Science* **1997**, *278*, 653.
(44) Journet, C.; Maser, W. K.; Bernier, P.; Loisseu, A.; Selachapelle, M. L.; Lefrant, S.; Deniard, P.; Lee, R.; Fischer, J. E. *Nature* **1997**, *388*, 756.
(45) Greiner, N. R.; Phillips, D. S.; Johnson, J. D.; Volk, F. *Nature* **1988**, *333*, 440.
(46) Bowen, C. R.; Derby, B. *Br. Ceramic Transactions* **1997**, *96*, 25.
(47) José-Yacamán, M.; Lopez, H.; Santiago, P.; Galván, D. H.; Garzón I. L.; Reyes, A. *Appl. Phys. Lett.* **1996**, *69*, 1065.
(48) Ugarte, D. *Nature* **1992**, *359*, 707.
(49) Banhart, F.; Ajayan, P. M. *Nature* **1996**, *382*, 433.
(50) (a) Curl, R. F.; Smalley, R. E. *Science* **1988**, *242*, 1017. (b) Curl, R. F.; Smalley, R. E. *Sci. Am.* **1991**, *October*, 32−41.
(51) Thess, A.; Lee, R.; Nikolaev, P.; Dai, H.; Petit, P.; Robert, J.; Xu, C.; Lee, Y. H.; Kim, S. G.; Rinzler, A. G.; Colbert, D. T.; Scruseria, G. E.; Tománek, D.; Fischer, J. E.; Smalley, R. E. *Science* **1996**, *273*, 483.
(52) Feldman, Y.; Tenne, R.; Hebben, M., to be published.
(53) (a) Feldman, Y.; Wasserman, E.; Srolovitz, D. J.; Tenne, R. *Science* **1995**, *267*, 222. (b) Srolovitz, D. J.; Safran, S. A.; Homyonfer, M.; Tenne, R. *Phys. Rev. Lett.* **1995**, *74*, 1778.
(54) (a) Furimsky, E.; Amberg, C. H. *Can. J. Chem.* **1975**, *53*, 3567. (b) Lee, W. L.; Besmann, T. M.; Stott, M. W. *J. Mater. Res.* **1994**, *9*, 1474.
(55) Staufer, U.; Wiesendanger, R.; Eng, L.; Rosenthaler, L.; Hidber, H. R.; Güntherodt, H.-J.; Garcia, N. *J. Vac. Sci. Technol., A* **1988**, *6*, 537.
(56) Shen, T. C.; Wang, C.; Abeln, G. C.; Tucker, J. R.; Lyding, J. W.; Avouris, P.; Walkup, R. E. *Science* **1995**, *268*, 1590.
(57) Frey, G. L.; Ilani, S.; Homyonfer, M.; Feldman, Y.; Tenne, R. *Phys. Rev. B* **1998**, *57*, 6666.
(58) *Standard Potentials in Aqeuous Solution*; Bard, A. J.; Parsons, R.; Jordan, J.; Eds.; Marcel Dekker: New York, 1985.
(59) Bonneau, P. R.; Jarvis, Jr R. F.; Kaner, R. B. *Nature* **1991**, *349*, 510.
(60) Zhang, Q. L., et al. *J. Phys. Chem.* **1986**, *90*, 525.
(61) Feldman, Y.; Frey, G. L.; Homyonfer, M.; Lyakhovitskaya, V.; Margulis, L.; Cohen, H.; Hodes, G.; Hutchison, J. L.; Tenne, R. *J. Am. Chem. Soc.* **1996**, *118*, 5362.
(62) Homyonfer, M.; Alperson, B.; Rosenberg, Yu.; Sapir, L.; Cohen, S. R.; Hodes, G.; Tenne, R. *J. Am. Chem. Soc.* **1997**, *119*, 2693.
(63) (a) Friend, R. H.; Yoffe, A. D. *Adv. Phys.* **1987**, *36*, 1. (b) Rouxel, J. *Curr. Sci.* **1997**, *73*, 31.
(64) Zelenski, C. M.; Dorhout, P. K. *J. Am. Chem. Soc.* **1998**, *120*, 734.
(65) Feldman, Y.; Lyakhovitskaya, V.; Tenne, R. *J. Am. Chem. Soc.* **1998**, *120*, 4176.
(66) (a) Grange, P. *Catal. Rev.-Sci. Eng.* **1980**, *21*, *1*, 135. (b) Spevack, Perry A.; McIntyre, N. S. *J. Phys. Chem.* **1993**, *97*, 11031.
(67) Margulis, L.; Dluzewski, P.; Feldman, Y.; Tenne, R. *J. Microscopy* **1996**, *181*, 68.
(68) (a) Hamada, N.; Sawda, S. I.; Oshiyama, A. *Phys. Rev. Lett.* **1992**, *68*, 1579. (b) Saito, R.; Fujita, M.; Dresselhaus, G.; Dresselhaus, M. S. *Appl. Phys. Lett.* **1992**, *60*, 2204. (c) Mintmire, J. W.; Dunlap, B. I.; Wjite, C. T. *Phys. Rev. Lett.* **1992**, *68*, 631.
(69) Bacon, R. *J. Appl. Phys.* **1960**, *31*, 283.
(70) Amelinckx, S., Bernaerts, D., Zhang, X. B., Van Tendeloo, G., Van Landuyt, J. *Science* **1995**, *267*, 1334.
(71) Sanders, J. V. *J. Electron Microscopy Technol.* **1986**, *3*, 67.
(72) Bursill, L. A. *Intl. J. Modern Phys. B* **1990**, *4*, 2197.
(73) Kroto, H. W. *Science* **1988**, *242*, 1139.
(74) Singer, I. L. "Solid lubrication processes" In *Fundamentals of Friction: Macroscopic and Microscopic Processes*; Singer, I. L.; Pollock, H. M., Eds.; Kluwer: Dordrecht, 1992; p 237.
(75) Zabinski, J. S.; Donley, M. S.; Dyhouse, V. J.; McDevitt, N. T. *Thin Solid Films* **1992**, *214*, 156.
(76) Landman, U.; Israelchvili, J. *Nature* **1996**.
(77) Rapoport, L.; Bilik, Yu.; Feldman, Y.; Homyonfer, M.; Cohen, S. R.; Tenne, R. *Nature* **1997**, *387*, 791.
(78) Vollath, D.; Szabó, D. V. *Mater. Lett.* **1998**, *35*, 236.

CM9802189